The Effect of Laser Shock Peening on Back Stress of Additively Manufactured Stainless Steel Parts

Veronica Over[1]
Department of Mechanical Engineering,
Columbia University,
500 W 120th St.,
New York, NY 10025
e-mail: vho2101@columbia.edu

Justin Donovan
Department of Mechanical Engineering,
Columbia University,
500 W 120th St.,
New York, NY 10025
e-mail: jmd2296@columbia.edu

Y. Lawrence Yao
Department of Mechanical Engineering,
Columbia University,
500 W 120th St.,
New York, NY 10025
e-mail: yly1@columbia.edu

This work studies the use of laser shock peening (LSP) to improve back stress in additively manufactured (AM) 316L parts. Unusual hardening behavior in AM metal due to tortuous microstructure and strong texture poses additional design challenges. Anisotropic mechanical behavior complicates application for mechanical design because 3D printed parts will behave differently than traditionally manufactured parts under the same loading conditions. The prevalence of back-stress hardening or the Bauschinger effect causes reduced fatigue life under random loading and dissipates beneficial compressive residual stresses that prevent crack propagation. LSP is known to improve fatigue life by inducing compressive residual stress and has been applied with promising results to AM metal parts. It is here demonstrated that LSP may also be used as a tool for mitigating tensile back-stress hardening in AM parts, thereby reducing anisotropic hardening behavior and improving design use. It is also shown that the method of application of LSP to additively manufactured parts is key for achieving effective back-stress reduction. Back stress is extracted from additively manufactured dog bone samples built in both XY and XZ directions using hysteresis tensile. Both LSPed and as-built conditions are tested and compared, showing that LSPed samples exhibit a significant reduction to back stress when the laser processing is applied to the sample along the build direction. Electron backscatter diffraction (EBSD) performed under these conditions elucidates how grain morphologies and texture contribute to the observed improvement. Crystal plasticity finite element (CPFE) modeling develops insights as to the mechanisms by which this reduction is achieved in comparison with EBSD results. In particular, the difference in plastic behavior across build orientations of identified crystal planes and grain families are shown to impact the degree of LSP-induced back-stress reduction that is sustained through tensile loading. [DOI: 10.1115/1.4056571]

Keywords: additive manufacturing, laser processes, modeling and simulation

1 Introduction

Laser shock peening (LSP) is typically used to process metal for fatigue life improvements in traditionally manufactured parts [1]. This process has been studied in detail for inducing compressive residual stress, which is responsible for arresting hairline fractures during fatigue loading and delaying stress corrosion cracking [2,3]. LSP also has a strong effect on dislocation structure and distribution causing a distinctive increase in geometrically necessary dislocation (GND) density in metal targets near the peened surface as well as a noticeable grain refinement and increased misorientation [4–7]. The dislocation shock waves produced by LSP have been observed to mitigate the tensile back stress of rolled stainless steel [8]. These authors have published finite element simulation results showing LSP processing causes bulk back-stress reduction via a highly localized compressive layer of back stress that overlaps with the compressive residual stress profile which LSP is known for introducing [8].

Laser shock peening is being investigated as a post-processing tool for additive manufacturing (AM) [9]. The effect of LSP on the measured tensile back stress of metal AM parts is as yet unstudied and is of particular interest due to the tortuous grain morphologies and dislocation distribution within 3D printed metal. The presence of back stress, also known as the Bauschinger effect, in AM steels is heightened due to both the high number of GNDs and dislocation cells in the as-built state and due to the heterogenous microstructure [10]. Parts with increased back stress display a lower resistance to random fatigue [11]. This is attributed to materials with high back stress developing a smaller plastically strained "shielding" volume which precedes ahead of cracks [12]. Therefore, materials with a high back stress have more catastrophic crack propagation and are thus more susceptible to weakening due to overloading and underloading [12]. Back stress also complicates analysis of fatigue life and spring-back causing challenges for failure design [13–15]. It is therefore desirable to investigate post-processing techniques such as LSP for the reduction of back stress.

Metal AM is poised to disrupt industry and in recent years both the public and private sector have increasingly been investing in progressing relevant technology [16]. Metal AM has the potential to radically reduce manufacturing waste and environmental impact as well as improve rapid prototyping processes and low-volume production [17]. Selective laser melting (SLM) or laser powder-bed fusion (LPBF) is hailed as one of the most promising forms of metal AM due to its high dimensional accuracy among other benefits [18]. However, this form of AM is still plagued by complications that act as stipulations for design. Artifacts of the build process include unique microstructural and mechanical characteristics that are introduced by the complex thermal history and temperature gradients occurring during fusion. In particular, dislocations are mired within unusual texture and microstructures to cause anisotropic properties.

The SLM build process produces both a high density of dislocations and directionally dependent internal structure, which causes back-stress hardening and subsequent challenges when fabricating

---

[1] Corresponding author.

Manuscript received September 8, 2022; final manuscript received December 15, 2022; published online January 19, 2023. Assoc. Editor: Cheryl Xu.

for structural use. The primary form of dislocation generation in 316L AM stainless steel has been attributed to thermal strain history and is affected by the rate of cooling, temperature gradient, and scanning strategy of printing [19,20]. Dislocation density is high within 3D printed steel—typically around 10^{13}–10^{14} m^{-2}, imparting both microscale and long-range stresses [19,21]. Grains near the melt-pool undergo plastic strain due to thermal expansion stresses and thus accumulate GNDs as they are forcibly confined by the surrounding material. Gradient microstructures, which have been linked to back-stress hardening, also occur inherently in AM steel [22,23]. Grain structure depends on the ratio of solidification rate to temperature gradient, causing either cellular or dendritic growth [24,25]. Grains tend to grow towards the centerline of the melt-pool, forming new grain boundaries at the surface. Cooling influences dendritic separation which also coincides with dislocation cell spacing in SLM metal [26]. Mosaic or "checker-board" macrostructures are often observed due to rotation of the scanning pattern between layers [27,28]. In builds with rotation between layers, the surface remelting of the previous layer causes epitaxial growth in the current build layer along the melt-pool boundaries of the previous layer [29]. The result is a pattern of rhomboid grain structures size of the melt-pool with larger central grains surrounded by smaller sub-grains. This variance of grain size based on location is characteristic of gradient microstructures and poses barriers to slip that encourage back-stress hardening. The prevalence of low-angle grain boundaries and solute segregation in AM stainless steel are also observed as providing significant obstacles to slip [30]. In situ observation of dislocations in loading–unloading–loading cycles of AM metal shows that GNDs tend to be annihilated upon unloading in a manner that is heightened at greater strains [31]. This behavior indicates the development of back stress during forward loading with mobile dislocations rebounding upon unloading to assist reverse yield. Strong crystallographic texture and grain elongation along the build direction (BD) further contribute to mechanical anisotropy [32]. Cubic crystal cells tend to grow either in a [100 or a 110 texture depending on the energy density used [22,33]. As a result of these properties, yielding and fatigue life vary according to the alignment of the loading direction (LD) to the building direction [34]. In particular, the back stress in SLM 316L is characterized as being distinctly tensile due to the metal's yield being stronger in tension than compression [21]. The presence of yield asymmetry due to back stress is a detriment to a part's fatigue behavior under selected loading conditions.

High residual stress is also prevalent and its distribution within 3D printed parts is contingent on the build orientation and parameter specification [21,35–37]. Residual stress forms in AM due to the temperature gradient mechanism in which the plastic expansion of a heated zone is confined by the surrounding material so that upon cooling there is a region of compressive residual stress surrounded by a zone of tensile residual stress [38]. This effect occurs when layers underneath the build layer are heated and cooled, resulting in a part with a core of compressive residual stress surrounded by an outer layer of tensile stress [38,39]. Residual stress profile and magnitude are dependent on scanning strategy and process parameters [37,40]. This residual stress can cause large part distortions, brittle fracture, a reduction in fatigue life, and susceptibility to stress corrosion cracking [41]. Stress can be alleviated by in situ heating of the build as well as various forms of post-processing such as hot-isostatic pressing, annealing, surface remelting, and LSP [36,42,43].

Solving the issues of residual stress, mechanical asymmetry and anisotropy improve the applicability of metal 3D printing technology to structural design. While many of these features are mitigated effectively by forms of annealing and hot-isostatic pressing, the side-effect is softening and it does not also induce beneficial properties [21,43,44]. LSP processing of AM metal has the potential to create advantageous compressive residual stress, improve fatigue life, and, as studied here, reduce tensile back stress. LSP has been investigated as both an in situ and post-processing technique for improving mechanical properties of AM parts [45,46]. The effects of the in situ process have been studied experimentally and through simulation, resulting in a beneficial compressive residual stress three-dimensional profile, deeply penetrating into the part [42,47]. It has also been shown to have promise in healing cracks during the build as well as closing pores [48,49]. As a post-processing mechanism for AM parts, many varied applications have been studied. It is shown that LSP induces a surface of refined grains and increased dislocation density as observed in traditionally manufactured parts [50]. It also has been shown to improve fatigue behavior of additively manufactured parts in a similar fashion to traditionally manufactured parts, namely, by producing compressive residual stress [51,52]. In one study, Lu et al. [53] found that LSP post-processing hardened and strengthened the specimens according to their build direction: in particular, horizontally built specimens were hardened and strengthened more than specimens built vertically. Lu et al. hypothesized that this is due to LSP increasing interlayer diffusion in horizontally built samples and decreasing the interlayer bonding in vertically built samples [53]. However, this analysis is currently untested and lacks observation of the interlayer micro-mechanics. Another effect produced by LSP post-processing has been observed upon annealing the AM and LSPed samples and examining the microstructure under the processed surface [54]. An investigation of the surface-level microstructure under the LSPed surface shows significant grain recrystallization after annealing with the dislocation cells produced by LSP serving as seeds for more equiaxed grain growth during heat treatment [54]. There is also some interest in using the residual stress produced by LSP to shape parts, allowing the deeply penetrating strain to curve metal parts back into their desired form [45]. The application of LSP to mitigate back stress in AM parts has potential as demonstrated by its previously studied effect on rolled stainless steel [8]. Due to the unique influences of microstructure and texture in AM metal, to further understand the effect of LSP, it is crucial to complement experiments with simulation methods that take these defining mechanisms into account.

The effect of LSP on back stress in AM parts is here quantified through hysteresis tensile testing and simulation. Of particular interest is the interaction of build orientation with the direction of LSP. Texture and microstructure are examined using electron backscatter diffraction (EBSD) before and after LSP as well as before and after 4% strain. Statistical regression shows that LSP only reduces back stress in samples aligned with the build direction. The cause of this reduction is examined through a multi-crystal rate-dependent crystal plasticity finite element (CPFE) simulation which factors in grain orientation, residual strain, and initial back stress.

2 Crystal Plasticity Modeling

CPFE models assess the influence of texture and microstructure upon the mechanical properties of a material and has been applied to AM structures. Given that so many aspects of the resultant AM part are dictated by build process, simulation allows parameter investigation which can provide insight into how to tailor the build for design use. Sub-grain formation and crystallization simulations articulate how process parameters directly affect the texture and structure [55,56]. CPFE simulation shows how this texture and structure affect bulk material properties. The mechanical effect of phase content and distribution within parts has been studied [57]. Polycrystalline CPFE has been used to quantify the effects of residual stress, back stress, microstructure morphology, and texture upon fatigue life, yielding, and stress–strain response [21,57–60]. These models tend to adhere to the basic form of CPFE in which grains are defined as either individual elements or groups of elements with an assigned crystal structure and orientation that reflects experimentally measured microstructure and texture. To model texture development, grain-specific strain, and back-stress hardening, this paper largely follows the crystal plasticity modeling by Chen et al. [21], which builds upon the work of Kalidindi et al. [61] and Asaro and Needleman [62]. Key relations and steps are briefly summarized here. A representative volume of 8000 elements is used. Each element in the model is an individual face-centered cubic (FCC) crystal and the resolved stress upon the element is solved using the Eshelby inclusion solution and therefore assumes equiaxed grains [63]. The use of equiaxed grains causes an underestimation of the back-stress hardening behavior because it would not capture the effect of aspect ratio on material properties. See Sec. 4.2 for more details. The use of equal-sized equiaxed grains is inherent to the solution mechanism due to volume averaging. The solution for translating the polycrystalline aggregate strain to slip system strain within each individual crystal follows Taylor's solution [64]. The FCC crystals are defined as having 12 {111}[110] slip systems each of which follow a rate-dependent hardening model. The plastic shearing rate follows a power law:

$$\dot{\gamma}_i^p = \dot{\gamma}_0^p \left|\frac{\tau_i - b_i}{s_i}\right|^{1/m} \mathrm{sgn}(\tau_i - b_i) \tag{1}$$

in which τ_i is the resolved shear stress, m is the strain rate sensitivity, S_i is the shear rate resistance, and $b_i = \boldsymbol{B}:\mathrm{sym}(\boldsymbol{m_i} \otimes \boldsymbol{n_i})$ a measure of back stress. The shear rate resistance evolves continuously and is conditional on the rate of slip causing the hardening law to be rate dependent:

$$\dot{s} = \sum\nolimits_j h_{ij} |\dot{\gamma}_j^p| \tag{2}$$

where

$$h_{ij} = q_{ij} h_0 \left(1 - \frac{s_j}{s_s}\right)^a \tag{3}$$

with q_{ij} the symmetric latent hardening matrix. The diagonal elements of q_{ij} are 1 while the off-diagonal elements are 1.4. The off-diagonal elements are the ratio of the latent hardening rate to the self-hardening rate. The hardening values are defined as the initial hardening rate $h_0 = 250$ MPa and the saturation resistance $s_s = 447$ MPa while $a = 0.023$. The measure of back stress is dependent on the slip system direction and normal vectors $\boldsymbol{m_i}$ and $\boldsymbol{n_i}$ as well as the back-stress tensor **B**. The back-stress tensor is calculated through integrating:

$$\dot{\boldsymbol{B}} = \sum_{j=1}^{12} h_b e^{-k\gamma_j^p} \dot{\gamma}_j^p \mathrm{sym}(\boldsymbol{m_j} \otimes \boldsymbol{n_j}) \tag{4}$$

In Eq. (4), h_b and k are material constants. Texture and residual strains are introduced into the model by assigning each grain of the representative volume a grain orientation and residual strain from measurements. While this model is unable to take into account the unusual grain shapes present in AM parts, assigning the model texture from EBSD scans enables simulation of the influence texture has upon the hardening behavior of the material, particularly the back stress. The back stress, strain, and texture can be extracted from each element according to grain family which allows comparison with EBSD results. Given that texture and grain rotation is a key method of plastic strain analysis, we must be able to identify typical modes of grain rotation using EBSD.

3 Experimental Methods

The effects of build orientation and LSP on the back stress, texture, and dislocation distribution of AM stainless steel were characterized using tensile testing, EBSD, and CPFE. Thirteen standard ASTM E8 dog bone samples were built using LPBF and 316L stainless steel powder. All dog bones had the same dimensions with outside dimensions 101.5 mm × 9.5 mm × 3.2 mm. Six samples were built in the *XY* orientation with the BD oriented along the axis of peening and seven samples were built in the *XZ* direction with the transverse direction (TD) oriented along the axis of peening (see Fig. 5). The LD is perpendicular to the TD and BD in both orientations. These build orientations will from now on and be referred to as *XY* and *XZ*. The build parameters are 0.04-mm layer thickness, energy densities of 57.7, 90 deg rotation between scan direction between layers, and 21–50 μm powder size. The front and back of the gauge length of all samples were mechanically polished followed by electropolishing. LSP was applied to the front and back of the gauge lengths of the test specimens. The test group composed of four of the *XY*-built and three of the *XZ*-built dog bones while three of the *XY*-built dog bones and three of the *XZ*-built dog bones were left untreated as control samples. The sample size asymmetry is due to laser availability for processing. A Spectra Physics Q-switched laser was used to peen the parts with a 700-μm diameter spot size set at 9.5 GW/cm^2 laser intensity. The pulse width is 10 ns and the repetition rate is 100 Hz. The LSP was applied with 75% overlap. The ablative coating used was 3M Polyester tape and the confining medium was 0.25-in.-thick clear acrylic. A method of hysteresis tensile loading developed by Yang et al. [23] and detailed in a previous study [8] was used to evaluate back stress. The unloading yield of the samples was defined as the point where the tangent modulus deviated from the unloading elastic modulus by 5%. The samples were pulled to 3% strain, unloaded, and reloaded to 4% strain. This range of loading captures the back stress at low plastic strain therefore best capturing the immediate hardening effects due to LSP. This range is also most relevant to low cycle fatigue. EBSD was performed before and after LSP and also before and after strain on the same grains.

4 Results and Discussion

4.1 Back-Stress Characterization. The LSPed samples exhibited a plastically deformed peen approximately 500 μm in diameter and 4 μm deep as measured by stylus profilometer. The polished surface of the material after peening shows uneven deformation along the indent boundaries. Tensile testing revealed that LSP consistently created a lower back stress in *XY* samples but did not do so consistently in *XZ* samples. The average back stress across all 13 samples is 149.81 ± 80.74 MPa. To ascertain that such a difference is statistically significant, the regression table shown in Table 1 is presented to show statistically significant differences in back stress between the *XZ* and *XY* builds. Two dummy variables are defined for build orientation (*XY* = 1), whether the sample has been LSPed (LSPed = 1) and an interaction term between the build orientation and whether the sample has been processed (*XY* * LSPed = 1). The table demonstrates that when considering a single variable at a time, the result seems to suggest that the effect of build direction is not significant enough ($p = 0.026$) nor the effect of LSP ($p = 0.251$). When these two variables are considered together, however, the *XY* * LSPed interaction term shows that LSPed samples built in the *XY* orientation have an effect on back stress at a high significance ($p < 0.01$).

Table 1 Regression table of analysis of variance showing the effect of build direction and LSP processing on the back stress measured by tensile testing

Variables	Coef.	95% conf. interval		*p*-value	Sig.
XY	128.75	19.39	238.1	0.026	**
LSPed	58.75	−50.61	168.1	0.251	–
XY * LSPed	−247.61	−403.2	−92.00	0.006	***
Constant	127.66	43.98	211.3	0.008	***
Mean dependent var		149.81	SD dependent var		80.74
R^2		0.68	Number of obs		13

Note: Dummy variables are defined as "*XY*" = 1 denotes the build is the *XY* orientation, "LSPed" = 1 indicates the sample is LSPed, and "*XY* * LSP" = 1 is an interaction term where the build orientation is *XY* and it is LSPed.
**$p < 0.05$.
***$p < 0.01$.

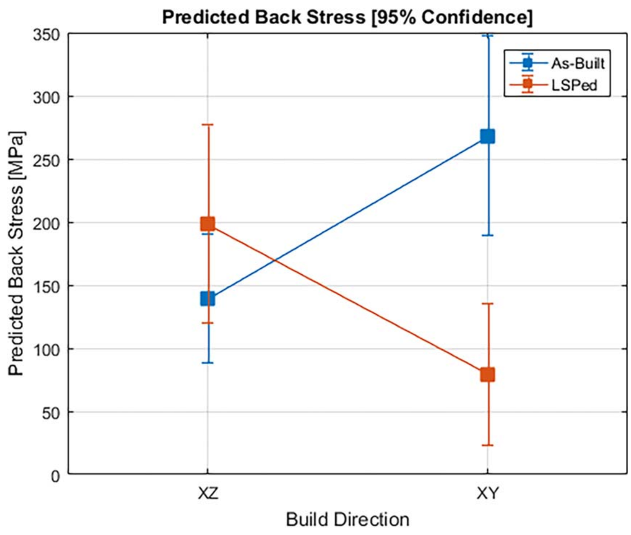

Fig. 1 Predicted average back stress for as-built and LSPed samples for both build directions holding manufacturer constant (manufacturer $2 = 0.62$). The 95% confidence intervals of the LSPed and as-built samples overlap significantly for the *XZ* samples but do not overlap for the *XY* samples. This shows that the build direction affects the ability of LSP to reduce back stress in additively manufactured parts.

Figure 1 depicts these results by showing the predicted means and 95% confidence interval of LSPed and as-built samples for both build orientations. As seen, there is significant overlap of the mean confidence intervals for LSPed and as-built samples built in the *XZ* orientation but not in the *XY* orientation. In the *XY* orientation, the lack of confidence interval overlap between processed and unprocessed means shows that there is a significant difference between the two. Furthermore, performing an *F*-test rejects the null hypothesis that the LSP dummy variables (LSPed and *XY** LSPed) have no effect upon the data at a 99% confidence. This reinforces that LSP statistically significantly affects back stress overall. As such, LSP is shown to significantly reduce the back stress of AM metal in the *XY*-build orientation but has no significant effect upon the *XZ*-built samples.

From this analysis, the effect that LSP has upon back stress is dictated by the orientation of the build with respect to loading and peening. Evidently, LSP only is able to achieve a significant back-stress reduction in *XY*-built samples and there is an interaction between the direction of peening, the direction of build, and the direction of loading. As previously discussed, Lu et al. [53] also noted that LSP had a stronger hardening and strengthening effect on tensile samples built in the *XY* orientation and peened in the BD than those built in the *XZ* orientation and peened in the TD. It is therefore unsurprising that the effect of LSP on back stress is also more pronounced for the *XY* orientation. While Lu et al. [53] theorize that this is due to layer bonding, they do not consider textural effects, nor do they examine the microstructural effects of different build orientations. To understand further the effect of build orientation on LSP-induced back-stress mitigation, EBSD is performed upon samples before and after LSP as well as before and after loading.

4.2 Texture and Microstructural Effects. The difference in response to LSP between the build orientations is rooted in the alignment of the direction of processing and tensile loading with the sample's internal anisotropy. The directionality of the microstructure is one of these contributing factors. Characteristic three-dimensional grain maps for the two build directions are shown in Figs. 2(*a*) and 2(*b*). As shown in Fig. 2, a distinct mosaic morphology dominates the samples and grains have an elongated structure along the BD. This morphology is oriented differently in the part according to build orientation so that in the *XY* build, the plane with mosaic structure is normal to the axis of peening, while in the *XZ* build it is perpendicular. The effect of elongated grains upon tensile back-stress development has been studied as the "aspect ratio effect" [65]. It has been shown that the higher the aspect ratio of a grain, the more back stress develops in transverse loading because of an increase in the number of obstacles to slip causing dislocation tangles. In the tested samples, the axis of tensile loading is oriented transversely to the elongated grain structure and contributes to heightened back-stress development. The orientation of the grain direction also affects the impact of LSP on the back stress of the different builds. The *XZ* samples have a larger number of grain boundaries acting as barriers to the plastic strain induced by LSP and thus should show less plastic strain after LSP than the *XY* samples.

The texture of the two build orientations, while similar along the BD, differs somewhat as shown in the pole figures in Figs. 2(*c*) and 2(*d*). While both samples demonstrate a moderate [220]/[110] texture along the BD, it is stronger in the *XZ* oriented samples than in the *XY* samples. A weaker [100] texture is identified along the TD for both builds. This texture makes the samples softest along the BD. The strongest texture is along the BD due to the columnar grains. The processing window used, specifically the energy density, does not create strong texture. The Schmid factor (m) for the texture is as follows: along the LD, $m = 0.447 \pm 0.043$; along the BD, $m = 0.465 \pm 0.030$; and along the TD, $m = 0.454 \pm 0.041$. The Schmid factor is calculated using the primary slip mode for FCC crystals namely $\{111\}[1\bar{1}1]$. Orientation imaging microscopy (OIM) analysis is used to calculate the average Schmid factors for stress application along different sample directions. For all scans, the BD axis of loading has a higher Schmid factor than the TD with the lowest Schmid factor along LD. We can thus expect more plastic rotation in the samples LSPed along the BD than those LSPed along the TD because the planes of slip are oriented to experience the most stress for loading along the BD. This hypothesis is tested to be correct by taking EBSD scans of the samples before and after LSP. Inverse pole figure (IPF) analysis shows that in both samples, the grains are oriented such that their planes of slip are clustered in a roughly stable configuration for tensile rotation of FCC crystals along the LD. These orientations are key for distribution of observable lattice rotation after loading especially at low strain.

The same grains were then scanned before and after LSP for both sample orientations, revealing differences in plastic response between *XY* and *XZ* samples. A difference pole figure demonstrating the change in texture due to LSP for the *XY* build is shown in Fig. 3(*a*). The *XY* texture shows greater plastic grain rotation due to LSP. The grain rotation is most pronounced in the [400]/[200] planes and then the [222]/[111] planes for both build orientations. However, the [220]/[110] planes also show some rotation. The plastic slip occurring in the *XY* build is observed to be more pronounced than in the *XZ* build. This is determined to be due to a combination of texture, microstructure, and anisotropy inherent to the build.

In addition, IPFs show the crystal planes that are oriented along a given direction and demonstrate key aspects of grain rotation in crystalline structures during tensile and compressive strain. Figure 4 illustrates the modes of rotation for FCC crystals. Under tension loading (Fig. 4(*a*)), the tensile axis of FCC crystals rotates towards the [101] direction until reaching the [001]–[111] line. Then a secondary mode of rotation occurs during which grains will rotate towards the [112] orientation [64]. During the initial mode of compression (Fig. 4(*b*)), the slip plane normal within FCC crystals will rotate to align with the compression axis, causing grains to rotate into the [001]–[110] symmetry line. The grains then enter the duplex slipping mode to rotate toward the [011] direction [64]. Deviations from these modes of slip for tension and compression loading imply additional microscale stresses that warp plastic strain behavior. These effects are to be observed in relation to build direction and LSP direction.

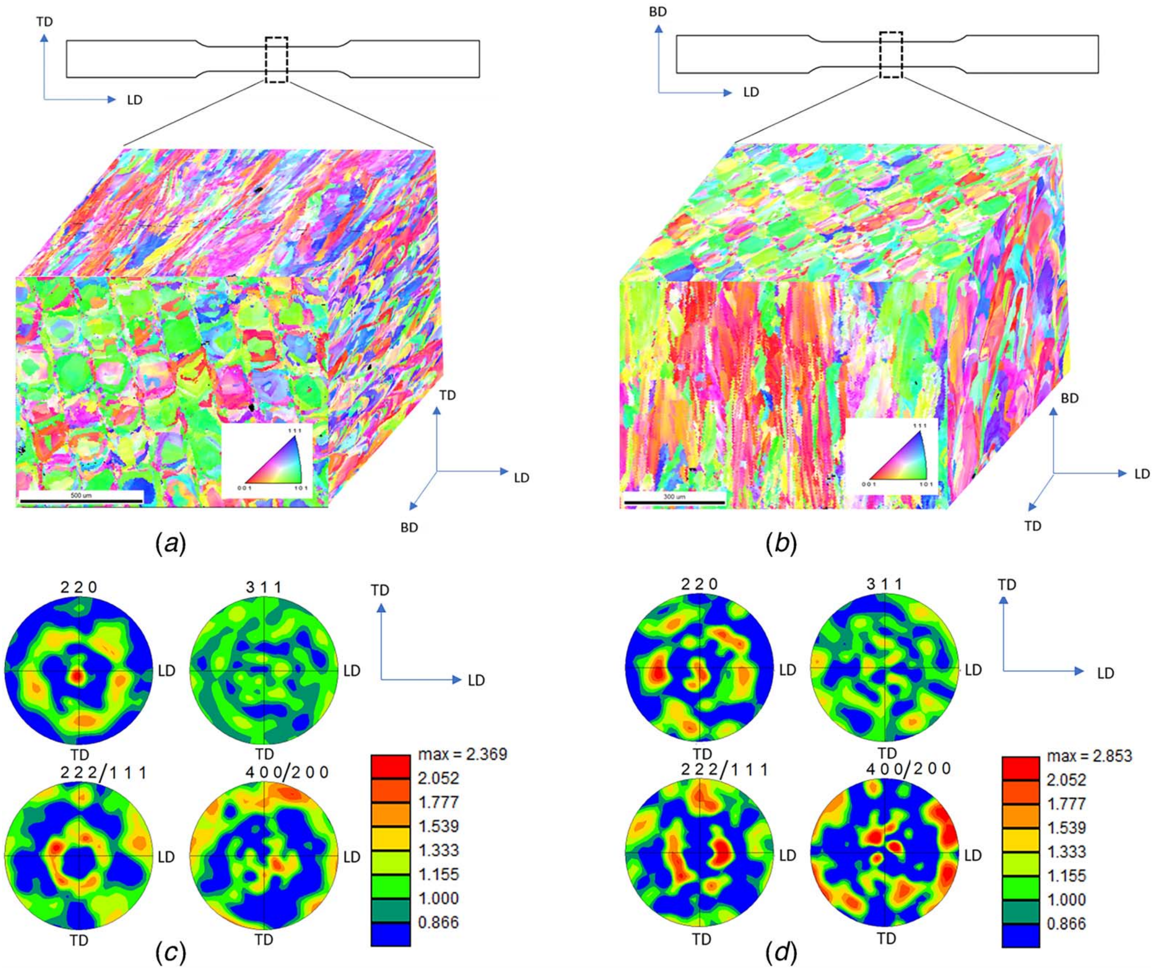

Fig. 2 Typical IPF maps of (*a*) the *XY*-build direction sample microstructure and (*b*) the *XZ*-build direction sample microstructure. Pole figures for grain families from EBSD in the (*c*) *XY*-build orientation and (*d*) *XZ*-build orientation. A strong [110] texture is evident along the build direction.

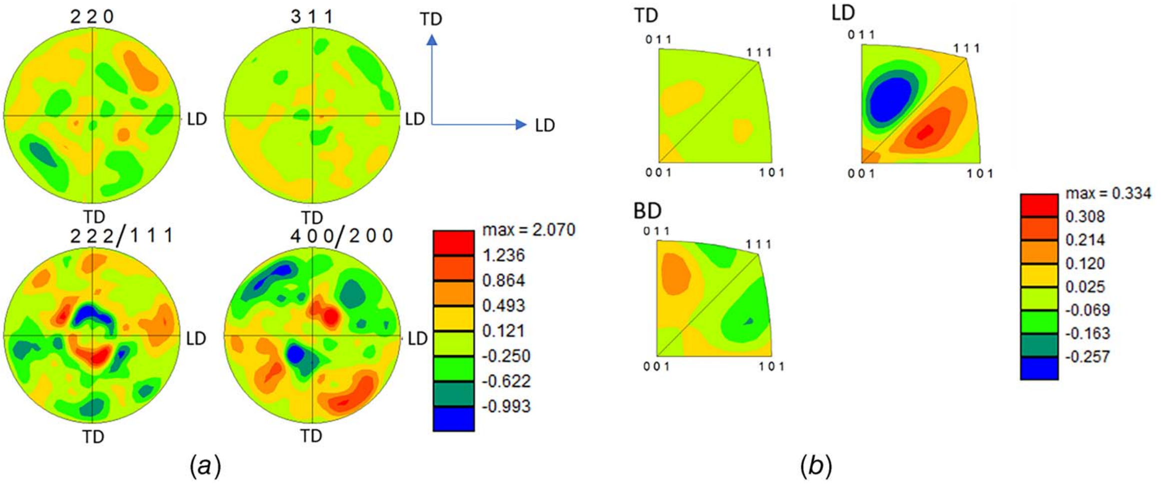

Fig. 3 A difference between textures is taken for the same group of grains and thus is able to show texture changes due to plastic deformation in a single plot. A higher intensity signifies a higher difference. This figure shows the change before and after LSP processing in the *XY*-build orientation shown with (*a*) difference pole figure and (*b*) difference IPF.

Figure 3(*b*) shows the IPF rotation after LSP in the *XY* build. The *XY* build showed a distinctively different response to LSP in the LD in comparison with the *XZ* build. The difference IPF along the LD shows that the *XY* samples exhibited a high rotation towards and across the [001]–[111] boundary line which has implication for subsequent tensile plastic deformation along the LD. Movement out of the [011]–[111]–[001] triangle reduces the Schmid factor for the primary slip mode [11−1](101) so that other modes of slip are more likely [66]. Meanwhile, the *XZ* build demonstrated characteristic compression grain rotation along the TD which is the axis of applied pressure after LSP with some smaller magnitude rotations in the LD and BD axes. It can be inferred that, due to the compression-stable orientation of the grains along the BD, applying pressure to the *XY*-build samples along the BD caused the most detectable grain rotation to be by modes of compression plastic strain beyond the secondary compression rotation mode which contributed to the high rotation in the LD. As studied by Chen et al. [67], LSP causes different rotation in grains according to their orientation. It is likely that the anisotropic intragranular features and grain morphology present in 3D printed samples will exacerbate these effects. Figure 3 shows that this strong tensile rotation of [222]/[111] and [400]/[200] planes in the LD primarily accounts for the larger magnitude of LSP-induced plastic rotation in the *XY* build as compared with the *XZ* build.

Comparison of the texture of LSPed and as-built samples before and after tensile loading demonstrates how LSP changes the mode of deformation in these samples. Samples experienced different grain rotation after 4% strain according to whether they had been LSPed or not. Characteristic difference IPFs as shown in Fig. 5 illustrate the different modes of grain rotation each of the samples experienced. The non-LSPed samples in both the *XY*- and *XZ*-build orientations display similar modes of grain rotation after tensile strain. Along the LD, the grains undergo the primary mode of FCC tensile grain rotation with rotation towards the [001]–[111] symmetry line. In the axes perpendicular to loading, the grains rotate along compression modes towards the [011] and [101] corners. The LSPed samples exhibit noticeably different grain rotation as exhibited in Fig. 5(*b*). The LSPed *XY* samples show compressive grain rotation in the LD. This is likely due to the compressive back stress and residual stress induced in the surface of the *XY* builds. The compressive back stress within the part is due to dislocation pile-ups at barriers to compressive strain. The compressive residual stress pins these dislocation pile-ups in place and as it is relaxed during loading, the compressive dislocations already formed encourage modes of grain rotation typically seen in compressive loading. LSP induced fewer pinned dislocations in the *XZ* build due to the texture's inherent hardness along the TD. As a result, the compressive rotation mode that is induced in the *XY* samples is not as pronounced in the *XZ* build.

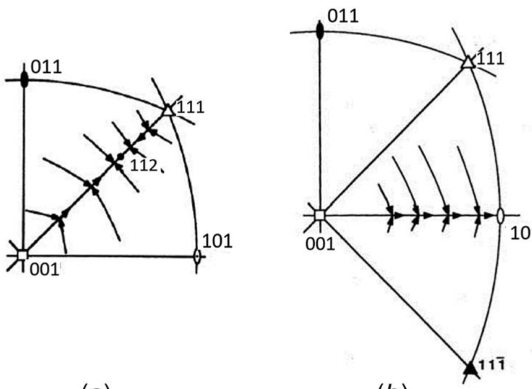

(*a*) (*b*)

Fig. 4 (*a*) Tension IPF rotation in an FCC crystal and (*b*) compression IPF rotation in an FCC crystal. Images adapted from Ref. [66].

This analysis is supported by the dislocations viewed in the *XY*- and *XZ*-build orientations before and after LSP. Dislocation density can be extracted from the EBSD images using OIM analysis to detect lattice curvature. Lattice curvature is directly proportional to GNDs and thus, given a known FCC primary slip system, we may extrapolate GND density. Figure 6 shows an increase in dislocation pile-ups near the grain boundaries after LSP for the same grains. It is evident from many such analyses of all sample conditions that LSP increases both the level and density gradient near the grain boundaries in the *XY* build by more than in the *XZ* build. The observed dislocation pile-ups contribute to a surface layer of compressive back stress that mitigates the field of tensile back stress developed during loading. These results support that the texture and microstructure of the metal interact with the direction of LSP and loading to produce significant back-stress reduction in the *XY* build and no observable effect in the *XZ* build. CPFE simulation of the texture is capable of demonstrating how back stress is developed for each orientation.

4.3 CPFE Simulation.

For CPFE simulation, each grain of the representative volume was assigned Bunge Euler angles randomly sampled from the grains of EBSD images. Figure 7 shows the orientation distribution of [110] planes as experimentally measured and compares it with the randomly sampled texture used in the representative volume. Though there is not an exact match of distribution, the strong [220]/[110] texture along the BD is still evident.

X-ray diffraction (XRD) was used to extract residual strains from the as-built samples to input by grain family into the simulation as well. A regression of the $\sin\psi^2$ versus the *d*-spacing with correction for the out-of-plane stresses allowed for residual stress and strain to be evaluated for all of the grain families in each build. Figure 8 shows a representative stress analysis. These residual strains are allocated to each grain family in the simulation grain by grain. To model the effect of texture on back-stress development, all representative volumes inherit the same back-stress tensor as was originally

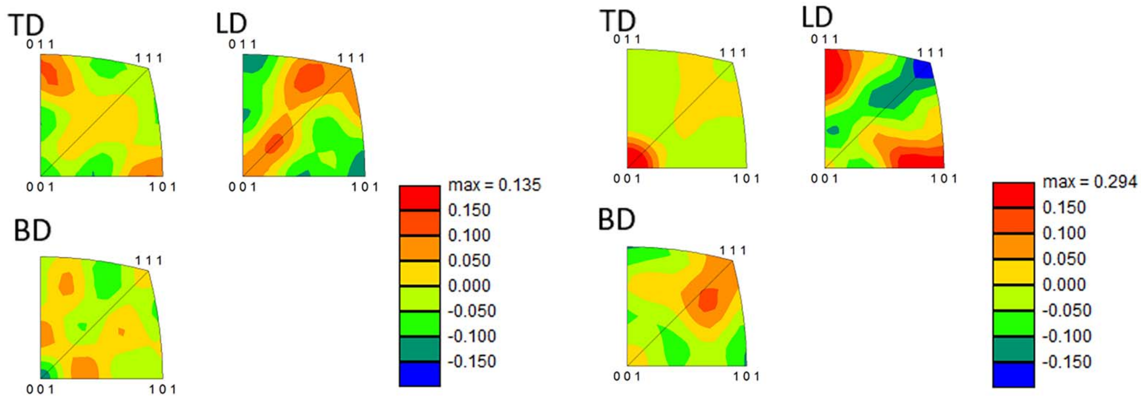

(*a*) (*b*)

Fig. 5 Characteristic difference IPFs showing the change before and after 4% strain for the (*a*) as-built *XY*-build orientation and (*b*) LSPed *XY*-build orientation

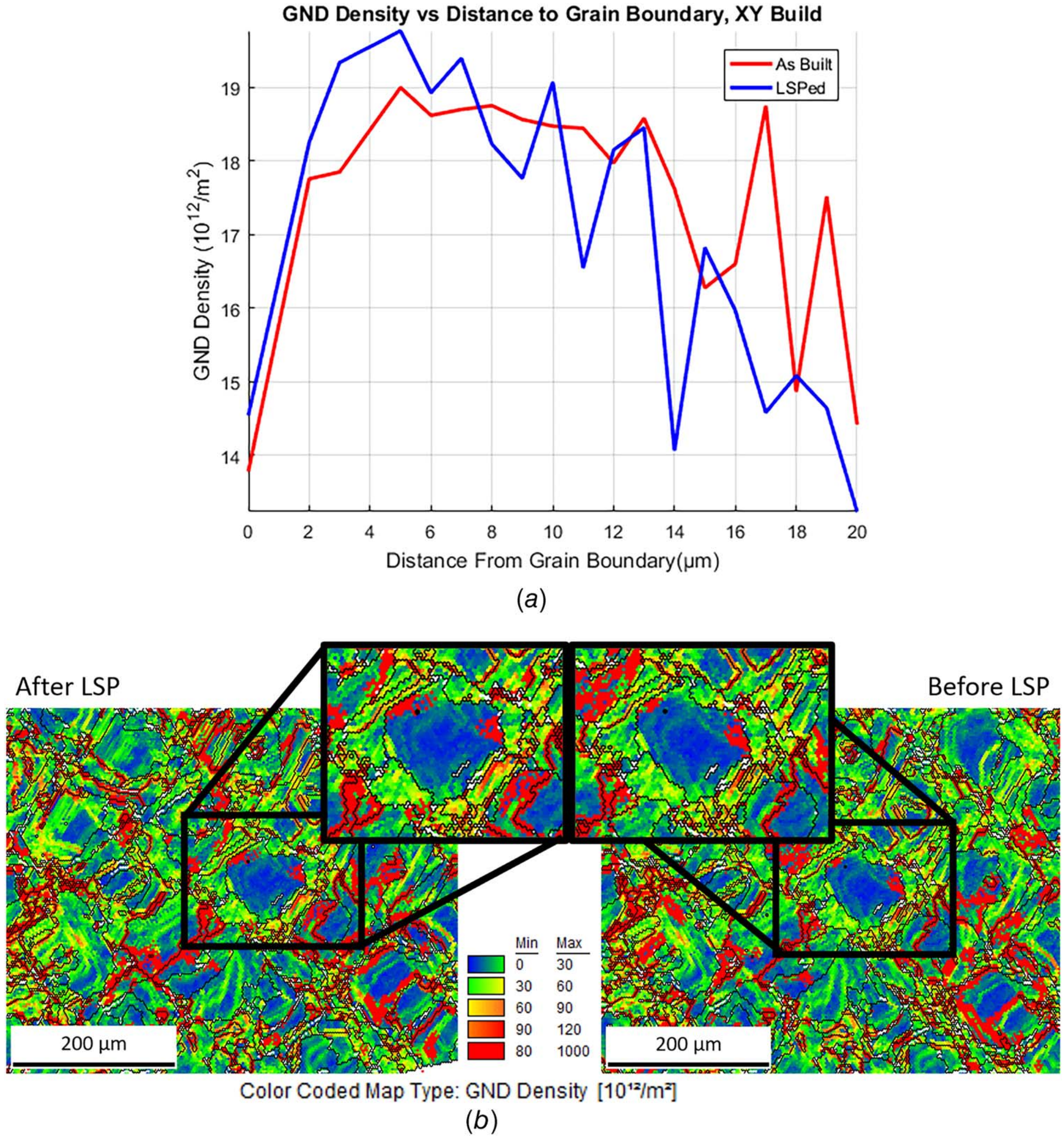

(*a*)

(*b*)

Fig. 6 (*a*) GND density versus distance to grain boundary before and after LSP for the same grains viewed in the TD–LD plane of the *XY*-build sample and (*b*) A sample scan showing the same grains before and after LSP highlighting the increased GND density gradient near the grain boundaries in the LSPed condition

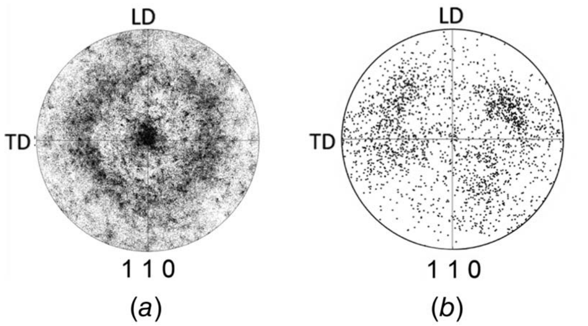

(*a*) (*b*)

Fig. 7 The experimentally measured texture in (*a*) compared with the texture used in simulation as shown in (*b*)

defined by Chen et al. [21]. A positive back stress of 30 MPa is applied in the LD and TD directions with a back stress of −60 MPa along the BD. Note that this initial back stress is applied across both build orientations to analyze the sole effect of texture and residual stress on back-stress hardening. To simulate back-stress development during tensile loading, a set velocity of 4 mm/s is defined on one plane of the representative volume while the opposite plane experiences a static boundary condition. The elastic strain of each grain family is extracted during this loading and the back stress of each grain family is evaluated as well. To simulate LSP, a gaussian spatial distribution of pressure with 2 GPa peak load is applied perpendicularly to the tensile loading direction. The pressure is applied so that it is ramped up to peak load at 5 ns and linearly decays to zero at 10 ns. The simulation is allowed to run so that the dislocations and stresses reach steady state before applying tensile loading.

Applying the sample texture measured by EBSD to CPFE enables simulation to approximate the hardening behavior of differently textured build orientations. Figure 9 shows the calculated CPFE effect of 4% tensile strain in the different build orientations alongside the experimentally measured difference pole figure demonstrating plastic grain rotation after 4% strain and unloading. CPFE accurately predicts the relative hardness of each of the grain families. Grain families are defined by the crystal plane normal that is most parallel with the peening direction. The

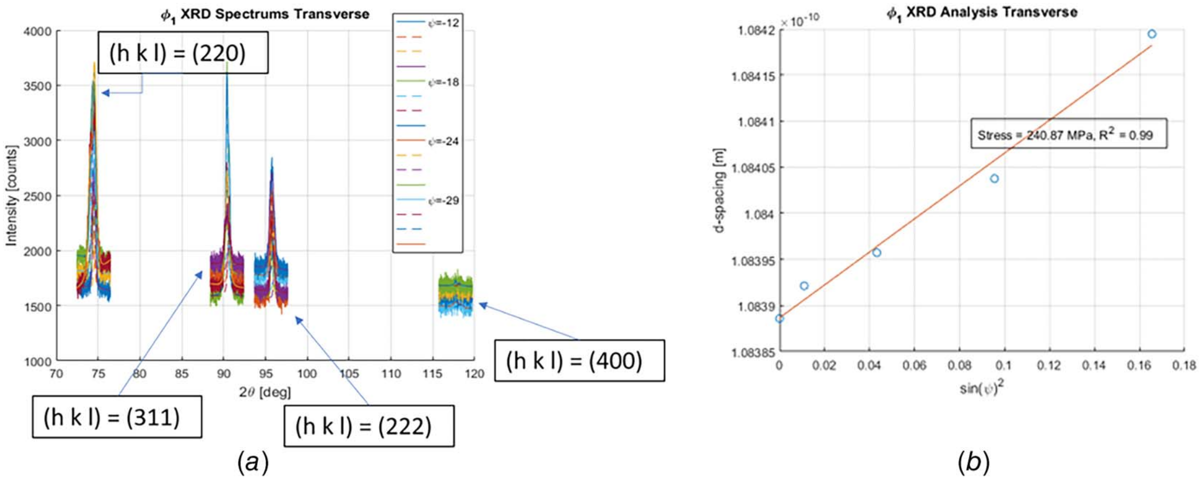

Fig. 8 (*a*) Plot of a representative sweep of XRD count intensity versus 2θ for different ψ angles and (*b*) the resultant stress analysis for the [222] lattice plane using linear regression of sin $^2(\psi)$ versus d-spacing data

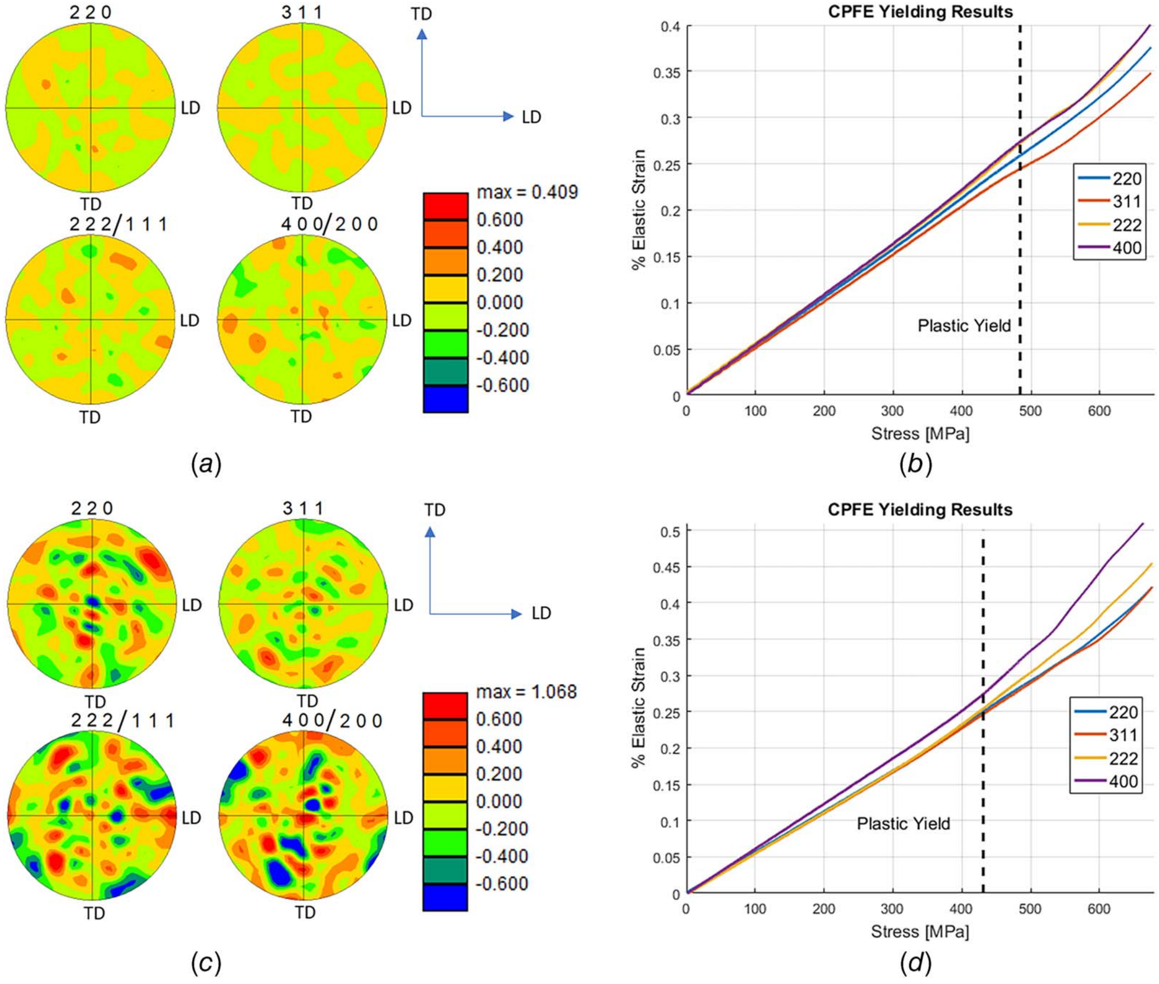

Fig. 9 EBSD results showing the difference pole figure change before and after 4% strain for the (*a*) as-built *XY*-build orientation and (*c*) as-built *XZ*-build orientation. CPFE elastic strain according to grain family after strain in (*b*) the *XY*-build orientation and (*d*) the *XZ*-build orientation.

CPFE reports that in both the *XY* and *XZ* orientations, the hardest grain family is the [311] grain family. The experimentally measured EBSD difference pole figure also identifies that the [311] planes are those that experience the least rotation. In the *XY*-build orientation, the next hardest grain family according to the CPFE is the [220] grain family which is corroborated by the EBSD results. The two softest grain families in the *XY*-build orientation are the [400]/[200] and the [222]/[111] grains. These planes are also the planes that yield the most according to the EBSD analysis. Difference pole figure analysis shows that the *XY*-build grain

Table 2 The average back stress from the LSPed CPFE simulation according to grain family after 4% tensile strain

	(220)	(311)	(222)	(400)
XY-build back stress	−12.0 MPa	−12.6 MPa	−16.2 MPa	−10.0 MPa
XZ-build back stress	5.72 MPa	0.38 MPa	6.91 MPa	16.6 MPa

families experience texture difference before and after 4% strain of 1.51, 1.14, 0.60, and 0.51 for the [400]/[200], [222]/[111], [220], and [311] grain families, respectively. The *XZ*-build orientation simulation exhibits the same hierarchy of material softness showing more plastic rotation in the [400]/[200] grain families than any of the other grain families. The *XZ*-built sample is also simulated to be significantly softer overall demonstrating that the stronger [220]/[110] texture contributes to the material's hardening behavior. Experimental EBSD confirms this fact with the texture difference before and after 4% strain of *XZ* samples being 12.02, 6.38, 2.96, and 2.45 for the [400]/[200], [222]/[111], [220], and [311] grain families, respectively. The hierarchy of grain rotation is again reflected well in the CPFE analysis. The [400]/[200] grain family shows the greatest strain followed by the [222]/[111] family. The [220] and [311] families show the least amount of strain. As can be seen from Fig. 9(*d*), the CPFE shows a wide strain difference between the [400]/[200] and [222]/[111] grain families which is mirrored by difference in the residual plastic rotation of the two grain families as shown by the EBSD difference pole figure: an intensity change of 12.02 is nearly twice as high as 6.38. Similarly, the [220] and [311] grain families are most similar in their CPFE cumulative strain and the change in the two families' textures are only different by 0.51 intensity. This method of comparison is a mode of validation of the hardening modeling of the CPFE.

CPFE back-stress analysis shows that the greater plastic strain exhibited by the *XZ* build resulted in an on average faster rate of back-stress development. The average back stress across all elements develops to 44.4 MPa in the *XZ* build after 4% strain compared with 38.4 MPa in the *XY* build. The higher rate of slip as exhibited by the [400]/[200] and [222]/[111] grain families in the *XZ* build drives higher back-stress development as shown with Eq. (4). On the other hand, in the *XY* build, the slip rate is roughly similar across all grain families. This effect has consequences for the interaction between LSP and build direction.

The LSPed simulation results show how the difference in hardening behavior of the [400]/[200] and [222]/[111] grain families between build directions contributes to the diminished effects of LSP on the *XZ* build as compared with the *XY* build. After LSP, the back stress along the loading direction is reduced significantly from 30 MPa to an average of −62.5 MPa and −75.0 MPa in the *XZ*-build and *XY*-build orientations, respectively. As seen experimentally in the EBSD analysis, the XY texture was softer to LSP resulting in greater compressive hardening. The increase in magnitude of compressive back stress due to LSP causes both orientations to begin yielding below 300 MPa of applied stress as compared with the unprocessed yielding behavior above 400 MPa as shown in Figs. 9(*b*)–9(*d*). However, the *XZ*-build back stress hardens more quickly than the *XY*-built samples. The average back stress after 4% strain is 8.55 MPa in the *XZ* build as compared with −11.9 MPa in the *XY* build. The *XY*-build direction retains a measure of compressive back stress through 4% loading which contributes towards an overall reduction of bulk back stress. As can be seen in Table 2, this is because of the unique hardening behavior of the [400]/[200] and [222]/[111] grain families in the *XZ*-build orientation. The texture of the *XZ* build favors a high rate of tensile plastic yield in these grain families and thus more rapidly hardens the overall build. This causes the effects of the LSP to be dissipated in the *XZ* build at a faster rate resulting in an experimentally non-observable difference between the LSPed and non-LSPed samples.

5 Conclusion

This work indicates that it is possible to induce lasting tensile back-stress reduction with LSP in additively manufactured stainless steel, given the build orientation and texture is chosen to be favorable. The *XZ*- and *XY*-built samples show statistically significant differences in measured back stress after LSP. While LSP does not have a significant effect on the *XZ*-built samples, it produces on average −247.61 MPa difference in *XY*-built samples all else equal. This study shows that the disparity in effect of LSP between build orientations is due to the following:

- Aligning the axis of peening along the BD causes LSP to compressively harden the surface material more, thereby reducing overall tensile back stress. Experimentally measured texture differences before and after LSP as well as CPFE simulation analysis show that LSP induces compressive hardening in *XY*-built samples due to the yielding of [400]/[200] and [222]/[111] planes which are positioned so as to be softer to peening along the build direction. Greater compressive plastic strain due to LSP causes heightened compressive back-stress hardening in the surface of the sample, resulting in an observable reduction to bulk tensile back stress.
- The texture of the *XZ*-built samples is softer to tensile loading along the pulling direction than that of the *XY*-built samples, causing tensile hardening to negate back-stress reduction in the LSPed *XZ* samples. EBSD analysis shows that [400]/[200] and [222]/[111] grain families are especially soft to tensile hardening in *XZ*-built samples. This is shown by the greater texture difference in these grain families before and after strain. The rapid hardening of the [400]/[200] and [222]/[111] grain families in the *XZ* samples dissipates the compressive back stress induced by LSP, leaving no observable difference between LSPed and non-LSPed samples.

Build orientation is therefore shown to interact with LSP to alter back stress and tensile hardening behavior in additively manufactured stainless steel parts. In particular, the metal's texture and the orientation of its texture with respect to loading and peening may either nullify the back-stress reduction due to LSP or sustain it through tensile strain.

Acknowledgment

Financial support from the NSF under grant #1761344 and the NSF graduate research fellowship is much appreciated. We acknowledge the Materials Research Science and Engineering Center funded by NSF at Columbia University for the use of its shared facilities. We thank Professor Yin Zhang of Georgia Tech for making the CPFE code available.

Conflict of Interest

There are no conflicts of interest.

Data Availability Statement

The datasets generated and supporting the findings of this article are obtainable from the corresponding author upon reasonable request.

References

[1] Clauer, A. H., 1996, "Laser Shock Peening for Fatigue Resistance," *Surface Performance of Titanium*, J. K. Gregory, H. J. Rack, and D. Eylon, eds., TMS, Warrendale, PA, pp. 217–30.

[2] Brandal, G., and Yao, Y. L., 2017, "Laser Shock Peening for Suppression of Hydrogen-Induced Martensitic Transformation in Stress Corrosion Cracking," ASME J. Manuf. Sci. Eng., **139**(8), p. 081015.

[3] Zhang, W., and Yao, Y. L., 2002, "Micro Scale Laser Shock Processing of Metallic Components," ASME J. Manuf. Sci. Eng., **124**(2), pp. 369–378.

[4] Lu, J. Z., Deng, W. W., Luo, K. Y., Wu, L. J., and Lu, H. F., 2017, "Surface EBSD Analysis and Strengthening Mechanism of AISI 304 Stainless Steel Subjected to Massive LSP Treatment With Different Pulse Energies," Mater. Charact., **125**, pp. 99–107.

[5] Clauer, A. H., and Holbrook, J. H., 1981, "Effects of Laser Induced Shock Waves on Metals," *Shock Waves and High-Strain-Rate Phenomena in Metals*, M. A. Meyers, and L. E. Murr, eds., Plenum Publishing Corporation, New York, pp. 675–703.

[6] Brandal, G., and Yao, Y. L., 2017, "Material Influence on Mitigation of Stress Corrosion Cracking Via Laser Shock Peening," ASME J. Manuf. Sci. Eng., **139**(1), p. 011002.

[7] Shadangi, Y., Chattopadhyay, K., Rai, S. B., and Singh, V., 2015, "Effect of Laser Shock Peening on Microstructure, Mechanical Properties and Corrosion Behavior of Interstitial Free Steel," Surf. Coat. Technol., **280**, pp. 216–224.

[8] Over, V., and Yao, Y. L., 2022, "Laser Shock Peening Induced Back Stress Mitigation in Rolled Stainless Steel," ASME J. Manuf. Sci. Eng., **144**(6), p. 061010.

[9] Kalentics, N., Boillat, E., Ciric-Kostic, S., Bogojevic, N., and Loge, R. E., 2017, "Tailoring Residual Stress Profile of Selective Laser Melted Parts by Laser Shock Peening," Addit. Manuf., **16**, pp. 90–97.

[10] He, X., Ye, Y. P., and He, B. B., 2022, "A Review on the Science of Plastic Deformation in Laser-Based Additively Manufactured Steel," J. Meter. Sci., **57**(24), pp. 10803–10835.

[11] Pommier, B., 2000, "Bauschinger Effect of Alloys and Plasticity-Induced Crack Closure: A Finite Element Analysis," FFEMS, **23**, pp. 129–139.

[12] Silva, F. S., 2007, "Fatigue Crack Propagation After Overloading and Underloading at Negative Stress Ratios," Int. J. Fatigue, **29**(9–11), 1757–1771.

[13] Barros, P. D., Alves, J. L., Oliveira, M. C., and Menezes, L. F., 2018, "Study on the Effect of Tension-Compression Asymmetry on the Cylindrical Cup Forming of an AA2090-T3 Alloy," Int. J. Solids Struct., **151**, 135–144.

[14] Charpentier, P. L., 2015, "Post-forming Monotonic and Cyclic Behavior in HSLA Steel Sheet After Large Deformations In-Plane Compression," Int. J. Fatigue, **79**, pp. 54–64.

[15] Chen, J., Yao, W., and Gao, D., 2020, "Fatigue Life Evaluation of Tension-Compression Asymmetric Material Using Local Stress-Strain Method," FFEMS, **43**(9), pp. 1994–2005.

[16] Grand View Research, 2019, "3D Printing Metal Market Size, Share & Trends Analysis Report By Product (Titanium, Nickel), By Form (Filament, Powder), By Application (Aerospace & Defense, Medical & Dental), By Region, and Segment Forecasts, 2021–2028."

[17] Frazier, W. E., 2014, "Metal Additive Manufacturing: A Review," ASM Int., **23**(6), pp. 1917–1928.

[18] Yap, C. Y., Chua, C. K., Dong, Z. L., Liu, Z. H., Zhang, D. Q., Loh, L. E., and Sing, S. L., 2019, "Review of Selective Laser Melting: Materials and Applications," Appl. Phys. Rev., **2**(4), p. 041101.

[19] Bertsch, K. M., Meric de Bellefon, G., Kuehl, B., and Thoma, D. J., 2020, "Origin of Dislocation Structures in an Additively Manufactured Austenitic Stainless Steel 316L," Acta Mater., **199**, pp. 19–33.

[20] Wang, G., Ouyang, H., Fan, C., Guo, Q., Li, Z., and Yan, W., 2020, "The Origin of High-Density Dislocations in Additively Manufactured Metals," Mater. Res. Lett., **4**(3), pp. 283–290.

[21] Chen, W., Voisin, T., Zhang, Y., Florien, J., Spadaccini, C. M., McDowell, D. L., Zhu, T., and Wang, Y. M., 2019, "Microscale Residual Stresses in Additively Manufactured Stainless Steel," Nat. Commun., **10**, p. 4338.

[22] Sun, Z., Tan, X., Tor, S. B., and Chua, C. K., 2018, "Simultaneously Enhanced Strength and Ductility for 3D-Printed Stainless Steel 316L by Selective Laser Melting," NPG Asia Mater., **10**(4), pp. 127–136.

[23] Yang, M., Pan, Y., Yuan, F., Zhu, Y., and Wu, X., 2016, "Back Stress Strengthening and Strain Hardening in Gradient Structure," Mater. Res. Lett., **4**(3), pp. 145–151.

[24] Paul, S., Liu, J., Strayer, S. T., Zhao, Y., Sridar, S., Klecka, M. A., Xiong, W., and To, C. A., 2017, "A Discrete Dendrite Dynamics Model for Epitaxial Columnar Grain Growth in Metal Additive Manufacturing With Application to Inconel," Addit. Manuf., **36**, p. 101611.

[25] Gorsse, S., Hutchinson, C., Goune, M., and Banerjee, R., 2017, "Additive Manufacturing of Metals: A Brief Review of the Characteristic Microstructures and Properties of Steels, Ti-6Al-4V and High-Entropy Alloys," Sci. Technol. Adv. Mater., **18**(1), pp. 1443–1465.

[26] Pauza, J. G., Tayon, W. A., and Rollett, A. D., 2021, "Computer Simulation of Microstructure Development in Powder-Bed Additive Manufacturing With Crystallographic Texture," Model. Simul. Mater. Sci. Eng., **29**(5), p. 055019.

[27] Moyle, M. S., Haghdadi, N., Liao, X. Z., Ringer, S. P., and Primig, S., 2022, "On the Microstructure and Texture Evolution in 17-4 *p*H Stainless Steel During Laser Powder Bed Fusion: Towards Textural Design," J. Mater. Sci. Technol., **117**, pp. 183–195.

[28] Saeidi, K., Kevetkova, L., Lofaj, F., and Shen, Z., 2016, "Novel Ferritic Stainless Steel Formed by Laser Melting From Duplex Stainless Steel Powder With Advanced Mechanical Properties and High Ductility," Mater. Sci. Eng.: A, **665**, pp. 59–65.

[29] Liu, C. Y., Tong, J. D., Jiang, M. G., Chen, Z. W., Xu, G., Liao, H. B., Wang, P., Wang, X. Y., Xu, M., and Lao, C. S., 2019, "Effect of Scanning Strategy on Microstructure and Mechanical Properties of Selective Laser Melted Reduced Activation Ferritic/Martensitic Steel," Mater. Sci. Eng.: A, **766**, p. 138364.

[30] Wang, Y. M., Voisin, T., McKeown, J. T., Ye, J., Calta, N. P., Li, Z., Zeng, Z., et al., 2017, "Additively Manufactured Hierarchical Stainless Steels With High Strength and Ductility," Nat. Mater., **17**, pp. 63–71.

[31] Zhang, X. X., Andra, H., Harjo, S., Gong, W., Kawasaki, T., Lutz, A., and Lahres, M., 2021, "Quantifying Internal Strains, Stresses, and Dislocation Density in Additively Manufactured AlSi10Mg During Loading-Unloading-Reloading Deformation," Mater. Des., **198**, p. 109339.

[32] Kok, Y., Tan, X. P., Wang, P., Nai, M. L. S., Loh, N. H., Liu, E., and Tor, S. B., 2018, "Anisotropy and Heterogeneity of Microstructure and Mechanical Properties in Metal Additive Manufacturing: A Critical Review," Mater. Des., **139**, pp. 565–586.

[33] Pham, M.-S., Dvgyy, B., Hooper, P. A., Gourlay, C. M., and Piglione, A., 2020, "The Role of Side-Branching in Microstructure Development in Laser Powder-Bed Fusion," Nat. Commun., **11**(1), p. 749.

[34] Im, Y.-D., Kim, K.-H., Jung, K.-H., Lee, Y.-K., and Song, K.-H., 2019, "Anisotropic Mechanical Behavior of Additive Manufactured AISI 316L Steel," Metall. Mater. Trans. A, **50**(4), pp. 2014–2021.

[35] Nadammal, N., Cabeza, S., Mishurova, T., Thiede, T., Kromm, A., Seyfert, C., Farahbod, L., Haberland, C., Schneider, J. A., Portella, P. D., and Bruno, G., 2017, "Effect of Hatch Length on the Development of Microstructure, Texture and Residual Stresses in Selective Laser Melted Superalloy Inconel 718," Mater. Des, **134**, pp. 139–150.

[36] Li, C., Liu, Z. Y., Fang, X. Y., and Guo, Y. B., 2018, "Residual Stress in Metal Additive Manufacturing," Proc. CIRP, **71**, pp. 348–353.

[37] Parry, L., Ashcroft, I. A., and Wildman, R. D., 2016, "Understanding the Effect of Laser Scan Strategy on Residual Stress in Selective Laser Melting Through Thermo-Mechanical Simulation," Addit. Manuf., **12**(A), pp. 1–15.

[38] Mercelis, P., and Kruth, J.-P., 2006, "Residual Stresses in Selective Laser Sintering," Rapid Prototyp. J., **12**(5), pp. 254–265.

[39] Tran, H. T., Chen, Q., Mohan, J., and To, A. C., 2020, "A New Method for Predicting Cracking at the Interface Between Solid and Lattice Support During Laser Powder Bed Fusion Additive Manufacturing," Addit. Manuf., **32**, p. 101050.

[40] Chen, S., Gao, H., Zhang, Y., Wu, Q., Gao, Z., and Zhou, X., 2022, "Review on Residual Stresses in Metal Additive Manufacturing: Formation Mechanisms, Parameter Dependencies, Prediction and Control Approaches," J. Mater. Res. Technol., **17**, pp. 2950–2974.

[41] Fang, Z.-C., Wu, Z.-L., Huang, C.-G., and Wu, C.-W., 2020, "Review on Residual Stress in Selective Laser Melting Additive Manufacturing of Alloy Parts," Opt. Laser Technol., **129**, p. 106283.

[42] Kalentics, N., Boillat, E., Peyre, P., Gorny, C., Kenel, C., Leinenbach, C., Jhabvala, J., and Loge, R. E., 2017, "3D Laser Shock Peening—A New Method for the 3D Control of Residual Stresses in Selective Laser Melting," Mater. Des., **130**, pp. 350–356.

[43] Sealy, M. P., Madireddy, G., Williams, R. E., Rao, P., and Toursangsaraki, M., 2018, "Hybrid Processes in Additive Manufacturing," ASME J. Manuf. Sci. Eng., **140**(6), p. 060801.

[44] Peng, X., Kong, L., Fuh, J. Y. H., and Wang, H., 2021, "A Review of Post-Processing Technologies in Additive Manufacturing," J. Manuf. Mater. Process., **5**(8), p. 38.

[45] Hackel, L., Rankin, J. R., Rubenchik, A., King, W. E., and Matthews, M., 2018, "Laser Peening: A Tool for Additive Manufacturing Post-Processing," Addit. Manuf., **24**, pp. 67–75.

[46] Munther, M., Martin, T., Tajyar, A., Hackel, L., Beheshti, A., and Davami, K., 2020, "Laser Shock Peening and Its Effects on Microstructure and Properties of Additively Manufactured Metal Alloys: A Review," Eng. Res. Express, **2**(2), p. 022001.

[47] Sealy, M. P., Madireddy, G., Li, C., and Guo, Y. B., 2016, "Finite Element Modeling of Hybrid Additive Manufacturing by Laser Shock Peening," Proceedings of the 27th Annual International Solid Freeform Fabrication Symposium, Austin, TX, Aug. 8–10, pp. 306–316.

[48] Kalentics, N., Sohrabi, N., Tabasi, H. G., Griffiths, S., Jamasp, J., Leinenbach, C., Burn, A., and Loge, R. E., 2019, "Healing Cracks in Selective Laser Melting by 3D Laser Shock Peening," Addit. Manuf., **30**, p. 100881.

[49] du Plessis, A., Glaser, D., Moller, H., Mathe, N., Tshabalala, L., Mfusi, B., and Mostert, R., 2019, "Pore Closure Effect of Laser Shock Peening of Additively Manufactured AlSi10Mg," 3D Print. Addit. Manuf., **6**(5), pp. 245–252.

[50] Guo, W., Sun, R., Song, B., Zhu, Y., Li, F., Che, Z., Li, B., Guo, C., Liu, L., and Peng, P., 2018, "Laser Shock Peening of Laser Additive Manufactured Ti6Al4V Titanium Alloy," Surf. Coat. Technol., **349**, pp. 503–510.

[51] Luo, S., He, W., Chen, K., Nie, X., Zhou, L., and Li, Y., 2018, "Regain the Fatigue Strength of Laser Additive Manufactured Ti Alloy Via Laser Shock Peening," J. Alloys Compd., **750**, pp. 626–635.

[52] Busi, M., Kalentics, N., Morgano, M., Griffiths, S., Tremsin, A. S., Shinohara, T., Loge, R., Leinenbach, C., and Strobl, M., 2021, "A Parametric Neutron Bragg Edge Imaging Study of Additively Manufactured Samples Treated by Laser Shock Peening," Sci. Rep., **11**(14919).

[53] Lu, J., Lu, H., Xu, X., Yao, J., Cai, J., and Luo, K., 2020, "High-Performance Integrated Additive Manufacturing With Laser Shock Peening-Induced Microstructural Evolution and Improvement in Mechanical Properties of Ti6Al4V Alloy Components," Int. J. Mach. Tools Manuf., **148**, p. 103475.

[54] Kalentics, N., Huang, K., Ortega Varela de Seijas, M., Burn, A., Romano, V., and Loge, R. E., 2019, "Laser Shock Peening: A Promising Tool for Tailoring Metallic Microstructures in Selective Laser Melting," J. Mater. Process. Technol., **266**, pp. 612–618.

[55] Pal, D., and Stucker, B., 2013, “A Study of Subgrain Formation in Al 3003 H-18 Foils Undergoing Ultrasonic Additive Manufacturing Using a Dislocation Density Based Crystal Plasticity Finite Element Framework,” J. Appl. Phys., **113**(20), p. 203517.

[56] Francois, M. M., Sun, A., King, W. E., Henson, N. J., Tourret, D., Bronkhorst, C. A., Carlson, N. N., et al., 2017, “Modeling of Additive Manufacturing Processes for Metals: Challenges and Opportunities,” Curr. Opin. Solid State Mater. Sci., **21**(4), 198–206.

[57] Kapoor, K., Yoo, Y. S. J., Book, T. A., Kacher, J. P., and Sangid, M. D., 2019, “Incorporating Grain-Level Residual Stresses and Validating a Crystal Plasticity Model of a Two-Phase Ti-6Al-4 V Alloy Produced Via Additive Manufacturing,” J. Mech. Phys. Solids, **121**, pp. 447–462.

[58] Lakshmanan, A., Yaghoobi, M., Stopka, K. S., and Sundararaghavan, V., 2022, “Crystal Plasticity Finite Element Modeling of Grain Size and Morphology Effects on Yield Strength and Extreme Value Fatigue Response,” J. Mater. Res. Technol., **19**, pp. 3337–3354.

[59] Acar, S. S., Bulut, O., and Yalcinkaya, T., 2022, “Crystal Plasticity Modeling of Additively Manufactured Metallic Microstructures,” Proc. Struct. Integr., **35**, pp. 219–227.

[60] Zhang, J., Li, J., Wu, S., Zhang, W., Sun, J., and Qian, G., 2022, “High-Cycle and Very-High-Cycle Fatigue Lifetime Prediction of Additively Manufactured AlSi10Mg Via Crystal Plasticity Finite Element Method,” Int. J. Fatigue, **155**, p. 106577.

[61] Kalidindi, S. R., Bronkhorst, C. A., and Anand, L., 1992, “Crystallographic Texture Evolution in Bulk Deformation Processing of FCC Metals,” J. Mech. Phys. Solids, **40**(3), pp. 537–569.

[62] Asaro, R. J., and Needleman, A., 1985, “Texture Development and Strain Hardening in Rate Dependent Polycrystals,” Acta Metall., **33**(6), pp. 923–953.

[63] Eshelby, J. D., 1957, “The Determination of the Elastic Field of an Ellipsoidal Inclusion, and Related Problems,” Proc. R. Soc. Lond., **241**(1226), pp. 376–396.

[64] Taylor, G. I., 1938, “Plastic Strain in Metals,” J. Inst. Metals, **62**, pp. 307–324.

[65] Espinosa, H. D., Panico, M., Berbenni, S., and Schwarz, K. W., 2006, “Discrete Dislocation Dynamics Simulations to Interpret Plasticity Size and Surface Effects in Freestanding FCC Thin Films,” Int. J. Plast., **22**(11), pp. 2091–2117.

[66] Hosford, W. F., 2010, *Mechanical Behavior of Materials*, Cambridge University Press, Cambridge. Chap. 7.

[67] Chen, H., Kysar, J., and Yao, Y. L., 2004, “Characterization of Plastic Deformation Induced by Microscale Laser Shock Peening,” ASME J. Appl. Mech., **71**(5), pp. 713–723.